COVER SHEET

Title: *Multiscale Failure Analysis of a 3D Woven Unit Cell Containing Defects for* Proceedings of the **American Society for Composites—Thirty-fifth Technical Conference**

Authors: Evan J. Pineda, NASA Glenn Research Center
Brett A. Bednarcyk, NASA Glenn Research Center
Trent M. Ricks, NASA Glenn Research Center
Babak Farrokh, NASA Goddard Space Flight Center
Wade Jackson, NASA Langley Research Center

ABSTRACT

Multiscale failure simulations have been performed for a Three-dimensional woven composite unit cell considering five, or more, length scales spanning the woven composite mesoscale to the sub-microscale voids. The multiscale recursive micromechanics approach, which enables recursive integration of general micromechanics theories over an arbitrary number of length scales, has been employed within the NASA Multiscale Analysis Tool. The multiscale model uses both the generalized method of cells and Mori-Tanaka micromechanics theories, and considers failure in the constituent materials using a simple damage model. Baseline results, containing distributed voids, are compared to uniaxial experimental data for an AS4 carbon fiber/ RTM6 epoxy matrix 3D orthogonal woven composite with good agreement in terms of global stiffness and global failure stress. The simulations demonstrate that the 3D woven composite exhibits damage tolerance through sustaining increasing axial load far beyond the first initiation of damage. The multiscale model is used to examine the nonlinear response of the material to other loading conditions. Case studies, motivated by X-ray computed tomography data, are presented on the effects of manufacturing induced voids and cracks.

Evan J. Pineda, Brett A. Bednarcyk, Trenton M. Ricks, Multiphysics and Multiscale Modeling, NASA Glenn Research Center, Cleveland, OH 44135, U.S.A.

Babak Farrokh, Mechanical Systems Analysis and Simulation Branch, NASA Goddard Space Flight Center, Greenbelt, MD 20771, U.S.A.

Wade Jackson, Durability, Damage Tolerance, and Reliability Branch, NASA Langley Research Center, Hampton, VA, 23681, U.S.A.

INTRODUCTION

Three-dimensional (3D) woven carbon fiber reinforced polymer (CFRP) composites are emerging as a viable aerospace material because of their observed damage tolerance and enhanced through-thickness properties, as compared to traditional layered composites [1-8]. Moreover, structures containing thick sections and/or complex geometries can fabricated using a single 3D woven preform that is infused with resin. Oftentimes, many morphological features, such as voids, cracks, disbonds, wrinkling/waviness of tows, variability in cross section of tows and tow misalignment, can be observed within the microstructure of the composites [9-12]. However, it is unclear whether these features are defects that affect the parts performance or if the overall response of the component is insensitive to the presence of these features. NASA's Composites Technology for Exploration (CTE) project, and other projects, have focused on both experimental and analytical campaigns to better understand these materials and improve the technology readiness level (TRL) of the materials as a replacement for heavy metallic ring-frames used to join adjacent stages in launch vehicles [12, 13].

As with most composite materials, the ability to perform virtual testing on 3D woven composites is highly beneficial to the overall development of the materials themselves and the design of structures utilizing these materials. The advantages of a virtual testing platform for 3D woven composites are compounded over traditional, laminated composites because of the ability to tailor the weave (meso-structure) and generate advanced geometries. Therefore, simulation tools for design, analysis, and manufacturing of 3D woven structures must be developed.

Progressive failure analysis (PFA) of 3D woven composites remains a challenge due to the complex geometry or the extremely fine meshes required to accurately capture the local fields. Thus, the extent of PFA simulations in the open literature is limited. Repeating unit cell (RUC) and mosaic FEM models of an idealized 3D weave geometry were used to predict the tensile strength in the warp-direction of notched and un-notched coupons with three different weaves [14, 15]. It has been shown that, an accurate representation of the mesoscale geometry can yield more accurate predictions [16]. A coupled multiscale model, wherein the tow is modeled with the N-layers concentric cylinder (NCYL) model, was used to predict progressive failure of a 3D woven composite under flexural loading [17]. Later, a similar multiscale model was used to model the tensile stress-strain response of a 3D woven dogbone specimen assuming different methods for creating the representative volume element (RVE) [18]. All the PFA models here predicted the strengths of un-notched coupons with good accuracy. However, significant error was observed in the strength predictions for the notched coupon [14]. It has been shown that tow misalignment has an effect on the compressive strength of 3D woven composites, and the digital element method was used to generate a realistic RVE containing imperfection in the tow paths and geometry which improved the predictions [19, 20]. An idealized representation of the mesostructured using a voxel mesh was used to model the failure of 3D woven bolted joints [21]. Recently, the progressive failure of a T-Joint was modeled using a mesoscale approach [22]. Finally, there has been some work to predict the response of 3D woven composites under loading conditions other than quasi-static, such as low velocity impact and high-rate loading [23-25]. Many of the models only considered the meso-architecture, and did not consider microstructure of the tows, even though matrix cracking in the tows can manifest into other relevant failure mechanisms such as tow splitting and/or disbonding.

Modeling of process induced defects or cracks has been limited. Hierarchical multiscale modeling utilizing the finite element method has been employed to study the effects of void content on the effective properties of the composite by reducing of randomly selected elements in the micro- and

mesoscales [26]. A thermal cooldown was applied to a 3D woven RVE and the resulting stress concentrations, due to mismatch in the coefficients of thermal expansion, we correlated to microcracks in an Xray-CT image [10]. A hierarchical multiscale modeling strategy has been used to capture the residual stresses due to the resin curing process [27]. The influence of tow crimp in 3D woven composites was studied using analytical rod and spring-based models [28].

Thus far, the trend in model development has been to increase the geometric fidelity of the model, which is on the critical path for development of a virtual testing platform for 3D woven composite structures [16, 18, 19, 29-35]. However, the computational cost of these models can be exorbitant as many the models contain upwards of hundreds of thousands, or even millions, of degrees of freedom. Of equal importance is the development of rapid engineering tools for material and structural design. With such tools, parametric and statistical studies can be conducted incorporating a variety of loading scenarios and levels of imperfections. Recently, the engineering constants for a 3D woven RUC were predicted utilizing the multiscale generalized method of cells (MsGMC) and were compared to voxel FEM model and experimental data—showing reasonable agreement with both [12].

The focus on the current work is to develop and validate a multiscale modeling tool capable of ultra-efficient analysis of a 3D woven composite RUC containing defects, including voids and cracks. The NASA Multiscale Analysis Tool (NASMAT), developed at the NASA Glenn Research Center, is the multiscale platform used to conduct the analysis [36]. Within NASMAT, the multiscale recursive micromechanics (MsRM) framework is employed which allows for the deployment of any of a variety of micromechanics theories, with a wide range of fidelity, at an arbitrary number of coupled length scales. To maintain ultra-efficiency in the computational cost, the generalized method of cells and Mori-Tanaka micromechanics theories to model the constituents and RUCs at the various scales in the model [37, 38].

The manuscript is organized as follows. First, there is a brief overview of the 3D woven composite experimental program of the CTE project which utilizes a building block approach. Next, details on the theoretical development of MsRM is presented. This is followed by a succinct description of NASMAT. Then, details are given on the multiscale model of the 3D woven RUC including defects. Finally, the results and discussion are presented, followed by future work.

EXPERIMENTAL PROGRAM

The objective of NASA's recent CTE project, under the Game Changing Development (GCD) program, within the Space Technology Mission Directorate (STMD), is to increase the TRL of bonded composite joints through testing and analysis. One focus of CTE is on 3D woven CFRP materials as a potential lighter-weight, damage tolerant, replacement for metallic ring-frames used to join the vertical stages of a launch vehicle.

A building block approach is taken towards the development of a 3D woven CFRP composite joint. Figure 1 one shows the tests conducted under this building block approach. Figure 1a shows an X-Ray CT image of a flat panel from which coupon specimens were cut and tested under tension and compression, room temperature/dry and elevated temperature/wet conditions, and single shear bearing [12]. In addition, acid digestion tests were conducted to ascertain the overall fiber volume fraction and void content. Figure 1b displays the C-chanel tension/compression test specimen that was designed to represent a relevant structural configuration containing a key engineering feature in a joint design, i.e., a bend with a sharp radius. Finally, the CAD model of the largest test specimen in the building block, the C-Joint sub-element, is presented in Figure 1c. The C-joint sub-element contains a honeycomb sandwich panel (blue) which represents the acreage of the launch vehicle

structure. This panel is bonded to the 3D woven C-rep flat section (magenta), which serves as a surrogate for the web in the C-channel, with a resin infused, 3D woven pi-preform and film adhesive (green). The C-joint sub-elements were tested at the NASA Marshall Space Flight Center (MSFC) under tension and compression. The specimen was mounted to an aluminum test stand and the load was introduced through an aluminum insert colored gray and yellow in Figure 1c, respectively.

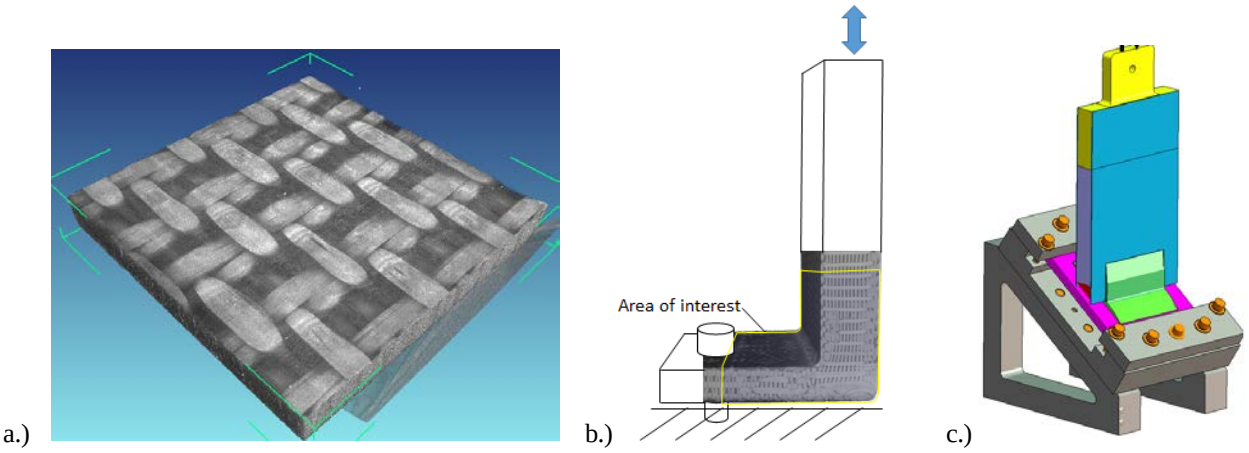

Figure 1. Building block approach for testing 3D woven composite structures. a.) Flat panel coupons. b.) C-channel. c.) C-joint sub-element containing honeycomb sandwich panel (blue), 3D woven C-rep panel (magenta), and 3D woven pi-preform (green).

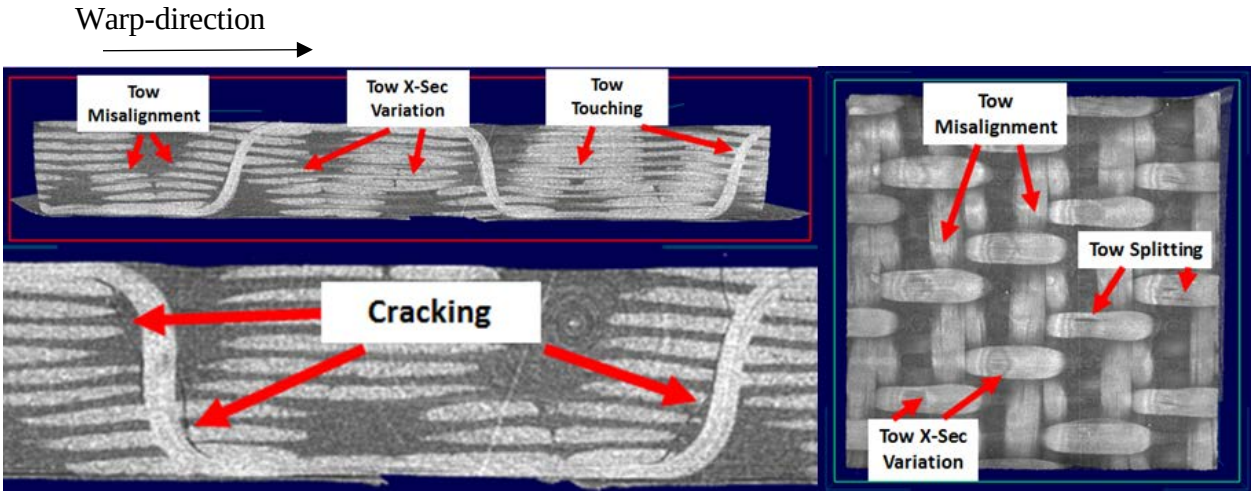

Figure 2. Pre-test X-Ray CT images of cross-section and through-section of 3D woven CFRP flat panel (SN005) exhibiting manufacturing-induced defects.

The CTE experimental program includes a thorough non-destructive evaluation (NDE) component which utilizes digital image correlation (DIC), X-Ray CT, acoustic emission (AE), and high-speed cameras to observe and monitor damage and manufacturing defects before, during and after testing. Figure 2 shows X-Ray CT images of the cross- and through-sections the SN005 flat panel which is the basis for the analysis in this work. Several manufacturing defects can be observed in Figure 2 including misaligned tows, variability in the cross-section (X-sec) of the tows, cracking in the bulk matrix near the binder tows, and splitting cracks in the binder tows. In Figure 3, two cross-

sectional images of the same C-channel specimen are displayed, and additional manufacturing defects are seen including voids, tow debonding, resin rich areas and surface cracks. For the C-channel, the most severe defects are found near the web to flange transition. It is clear from Figure 2 and Figure 3, that the manufacturing-induced defects in these 3D woven composites are substantial. However, it is ambiguous as to the effect of these anomalies on the overall behavior of the component. As described previously, very little computational modeling has been conducted to understand these effects. A focus of the present work is to understand the effects of some of these manufacturing induced irregularities.

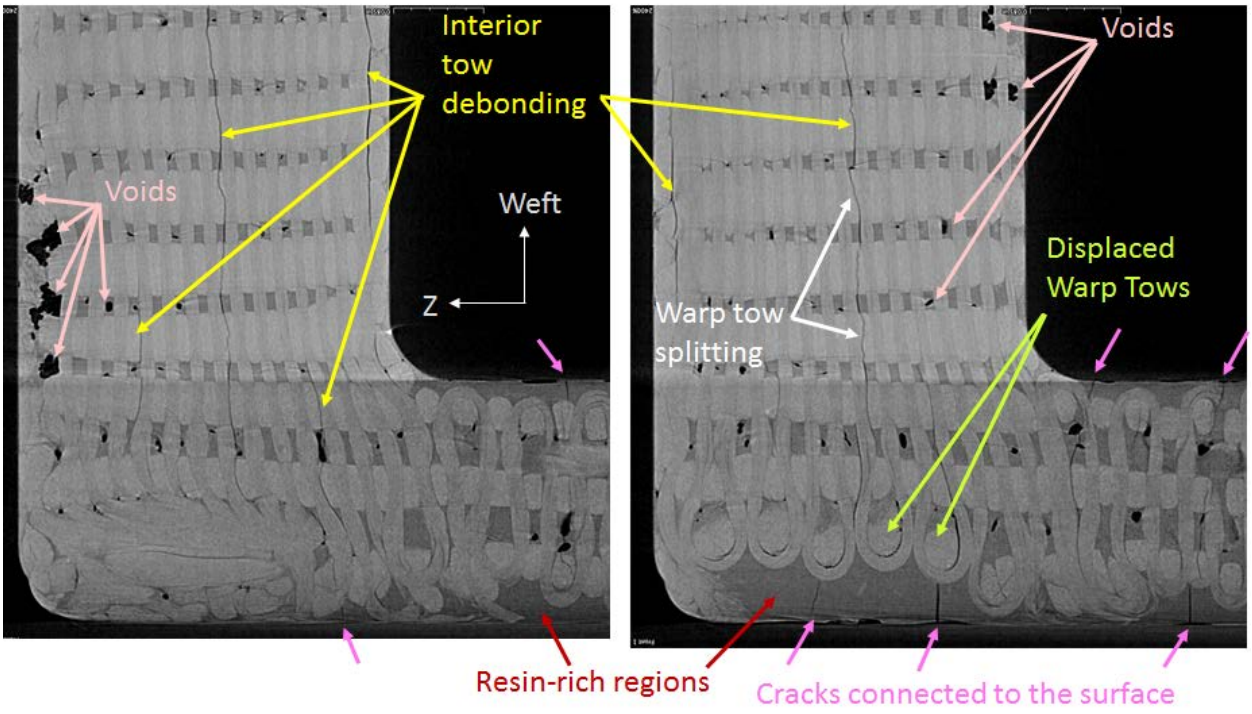

Figure 3. Pretest X-Ray CT images of cross-section of C-channel coupon specimen exhibiting manufacturing-induced defects.

MULTISCALE RECURSIVE MICROMECHANICS

The MsRM approach for modeling materials with multiscale microstructures is shown schematically in Figure 4. The computational implementation of this approach relies on recursive procedures, subroutines, and data structures that allow an arbitrary number of scales to be defined and seamlessly pass data between each other. The approach admits any micromechanics theory that provides a strain concentration tensor $\mathbf{A}_i^{(\alpha_i)}$, which relates the local strains within subvolumes in the material to the global strains, with the subvolumes (at a given scale, i) denoted in general by α_i, and the number of subvolumes by N_{α_i} This concentration tensor provides the local strains in the subvolumes in terms of the average (global) strains, $\overline{\boldsymbol{\varepsilon}}_i$,

$$\boldsymbol{\varepsilon}_i^{(\alpha_i)} = \mathbf{A}_i^{(\alpha_i)} \overline{\boldsymbol{\varepsilon}}_i \tag{1}$$

Substituting Eq. (1) into the local constitutive equation,

$$\boldsymbol{\sigma}_i^{(\alpha_i)} = \mathbf{C}_i^{(\alpha_i)} \boldsymbol{\varepsilon}_i^{(\alpha_i)} \tag{2}$$

gives,

$$\boldsymbol{\sigma}_i^{(\alpha_i)} = \mathbf{C}_i^{(\alpha_i)} \mathbf{A}_i^{(\alpha_i)} \overline{\boldsymbol{\varepsilon}}_i \tag{3}$$

The average (global) stress tensor is given by,

$$\overline{\boldsymbol{\sigma}}_i = \sum_{\alpha_i=1}^{N_{\alpha_i}} v_{\alpha_i} \boldsymbol{\sigma}_i^{(\alpha_i)} \tag{4}$$

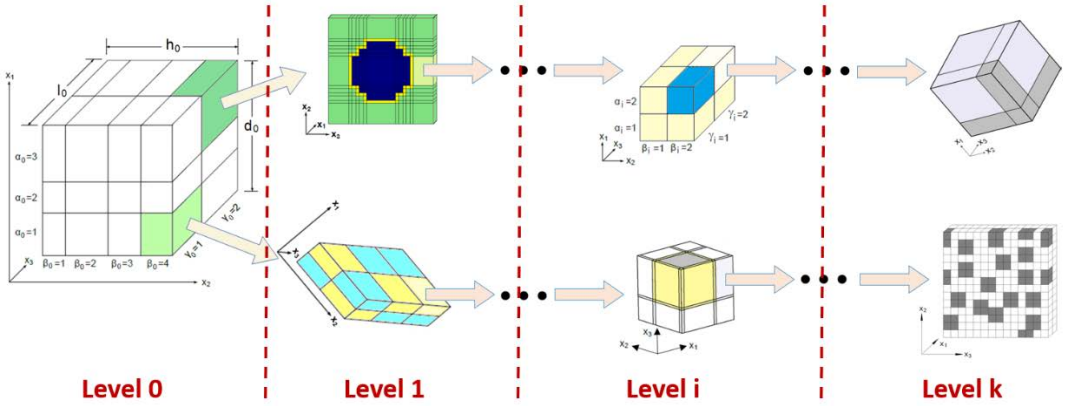

Figure 4. Schematic of the Multiscale Recursive Micromechanics (MsRM) approach wherein micromechanics models are embedded within each other to model microstructure at any number of length scales.

where v_{α_i} is the volume fraction of subvolume α_i. Eqs. (3) and (4) lead to,

$$\overline{\boldsymbol{\sigma}}_i = \sum_{\alpha_i=1}^{N_{\alpha_i}} v_{\alpha_i} \mathbf{C}_i^{(\alpha_i)} \mathbf{A}_i^{(\alpha_i)} \overline{\boldsymbol{\varepsilon}}_i \tag{5}$$

and recognizing that the effective elastic constitutive equation at level *i* is given by,

$$\overline{\boldsymbol{\sigma}}_i = \mathbf{C}_i^* \overline{\boldsymbol{\varepsilon}}_i \tag{6}$$

Eqs. (5) and (6) indicate that the effective stiffness tensor, $\mathbf{C}_i^*$, at level *i* is given by,

$$\mathbf{C}_i^* = \sum_{\alpha_i=1}^{N_{\alpha_i}} v_{\alpha_i} \mathbf{C}_i^{(\alpha_i)} \mathbf{A}_i^{(\alpha_i)} \tag{7}$$

In MsRM, the scales are linked by equilibrating the homogenized average stress, strain, and stiffness tensors at Level *i* to the local stress, strain, and stiffness tensors of a given subvolume at Level *i*-1 (with appropriate transformation to account for the potential coordinate system change from scale to scale). That is,

$$\overline{\boldsymbol{\varepsilon}}_i = \mathbf{T}_2^i \, \boldsymbol{\varepsilon}_{i-1}^{(\alpha_{i-1})}, \qquad \overline{\boldsymbol{\sigma}}_i = \mathbf{T}_2^i \, \boldsymbol{\sigma}_{i-1}^{(\alpha_{i-1})}, \qquad \mathbf{C}_i^* = \mathbf{T}_4^i \, \mathbf{C}_{i-1}^{(\alpha_{i-1})}, \qquad i = 1, \ldots, k \tag{8}$$

where $\mathbf{T}_2^i$ and $\mathbf{T}_4^i$ are the appropriate second and fourth order coordinate transformation tensors, respectively. Hence, it is clear that starting with the lowest scale (*k*) microstructure (see Figure 1), whose subvolumes contain only monolithic materials, the effective stiffness tensor can be calculated using any standard micromechanics theory. This stiffness tensor (after appropriate coordinate transformation) then represents the homogenized material occupying one of the subvolumes within a composite material at the next higher length scale. Given the transformed effective stiffness tensors of all subvolumes at this next higher length scale, the effective stiffness tensor of the composite at this level can be determined. This stiffness tensor can then be transformed and passed along to the next higher length scale, and the process repeats until the highest length scale considered (0) is reached.

As an example, for an MsRM analysis considering three length scales (0, 1, and 2), the overall effective stiffness tensor can be written using Eqs. (7) and (8) as,

$$\mathbf{C}_0^* = \sum_{\alpha_0} v_{\alpha_0} \left\{ \left(\mathbf{T}_4^1 \right)^{-1} \sum_{\alpha_1} v_{\alpha_1} \left[\left(\mathbf{T}_4^2 \right)^{-1} \sum_{\alpha_2} v_{\alpha_2} \mathbf{C}_2^{(\alpha_2)} \mathbf{A}_2^{(\alpha_2)} \right]^{(\alpha_1)} \mathbf{A}_1^{(\alpha_1)} \right\}^{(\alpha_0)} \mathbf{A}_0^{(\alpha_0)} \tag{9}$$

Note that in Eq. (9), the superscript on the bracketed terms indicates that all variables within the brackets are a function of the subvolume indices from the next higher length scale (including lower scale volume fractions and subvolume indices). The intent of this notation is to fully define the subvolume at a given scale as one progresses down the length scales. For example, using this notation, the effective stiffness tensor at level 2, from Eq. (8), can be written as,

$$\left\{ \left[\mathbf{C}_2^* \right]^{(\alpha_1)} \right\}^{(\alpha_0)} = \left\{ \left[\mathbf{T}_4^2 \right]^{(\alpha_1)} \right\}^{(\alpha_0)} \left\{ \mathbf{C}_1^{(\alpha_1)} \right\}^{(\alpha_0)} \tag{10}$$

as there are distinct $\mathbf{C}_2^*$ values for every level 1 subvolume, while there are distinct level 1 composites present within each level 0 subvolume.

Converse to this multiscale homogenization procedure, MsRM can perform multiscale localization of the stress and strain tensors. The multiscale localization is needed for inclusion of nonlinearity from damage (and inelasticity). For the three length scale example, the local strain tensor in an arbitrary lowest scale (level 2) subvolume can be written using Eqs. (1) and (8) as,

$$\left\{ \left[\boldsymbol{\varepsilon}_2^{(\alpha_2)} \right]^{(\alpha_1)} \right\}^{(\alpha_0)} = \left\{ \left[\mathbf{A}_2^{(\alpha_2)} \right]^{(\alpha_1)} \right\}^{(\alpha_0)} \left\{ \left[\mathbf{T}_2^2 \right]^{(\alpha_1)} \right\}^{(\alpha_0)} \left\{ \mathbf{A}_1^{(\alpha_1)} \right\}^{(\alpha_0)} \left\{ \mathbf{T}_2^1 \right\}^{(\alpha_0)} \mathbf{A}_0^{(\alpha_0)} \overline{\boldsymbol{\varepsilon}}_0 \tag{11}$$

Again, the superscript on the bracketed terms indicates that all variables within the brackets are a function of the subvolume indices from the next higher length scale. The stress tensor for any subvolume at any length scale can be similarly determined through localization, or by simply using the strain tensor, along with the constitutive equation (2), at the appropriate length scale. Note that, although not shown here for simplicity, the MsRM implementation in NASMAT includes thermal stresses as well. Because of its ability to handle multiple length scales in a single analysis, MsRM is ideal for multiscale modeling of materials such as 3D woven composites that exhibit identifiable microstructures across multiple length scales.

MULTISCALE MODEL OF 3D WOVEN COMPOSITE UNIT CELL IN NASMAT

The recent development of NASMAT has focused on modularity, upgradability and maintainability, interoperability, and utility [36]. The various operations of the code are compartmentalized into a finite set of procedures each of which is accompanied with a library of modules. Specific modules can be swapped, in and out as needed, to solve the particular multiscale problem of interest. Numerous procedures, and the subroutines used within the modules, are recursive. Moreover, recursive data types are used extensively to handle the large quantities of data associated with each length scale. The recursive nature of the NASMAT procedures and data enabled the development of the MsRM framework capable of supporting massively multiscale modeling (M^3) on high performance computing systems (HPC). Finally, application program interfaces (APIs) have been developed to support communication between NASMAT and other external programs.

MsRM Hierarchy of baseline SN005 3D woven model

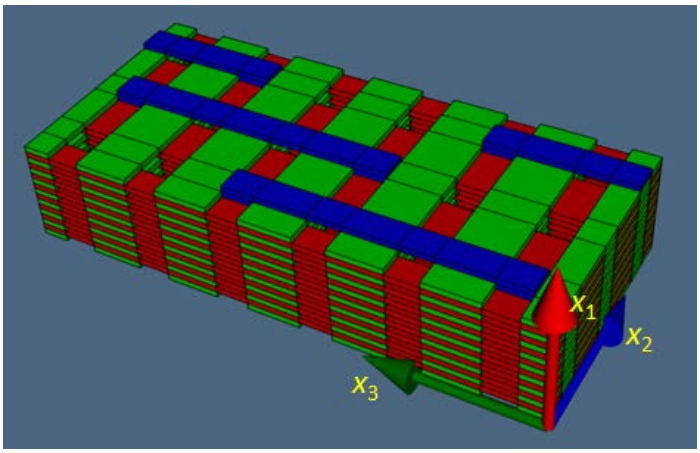

Figure 5. Idealized geometry of 3D woven SN005 RUC used to generate MsRM model in NASMAT. Only the warp (red), weft (green), and binder (blue) tow representations are displayed and the bulk matrix is omitted.

A multiscale model of the SN005 3D orthogonal woven RUC was generated in NASMAT using the idealized geometry given in Figure 5, where the bulk matrix is omitted to display the red warp, green weft, and blue binder tows, and analyzed with the MsRM implementation Figure 6 shows the overall MsRM RUC hierarchy deployed to model the 3D woven RUC. It can be seen that the analysis spans six length scales. Since NASMAT facilitates an integrated approach, homogenization and localization occurs across all scales at each time step to compute the macroscopic non-linear response

of the RUC. Far field applied strains are passed down from above. Periodic boundary conditions are assumed for every RUC at every scale, and homogenization is performed at every scale to provide the mechanical properties for the appropriate material point at the higher scale.

The MsRM framework is agnostic with respect to the specific micromechanics theory used. Hypothetically, any micromechanics theory can be used at any scale in an MsRM analysis. This allows for tailoring of the solution methodology to optimize the balance between efficiency and fidelity. Here a mixture of the doubly-periodic GMC, triply periodic GMC, and MT were utilized, as shown in Figure 6 [37, 38].

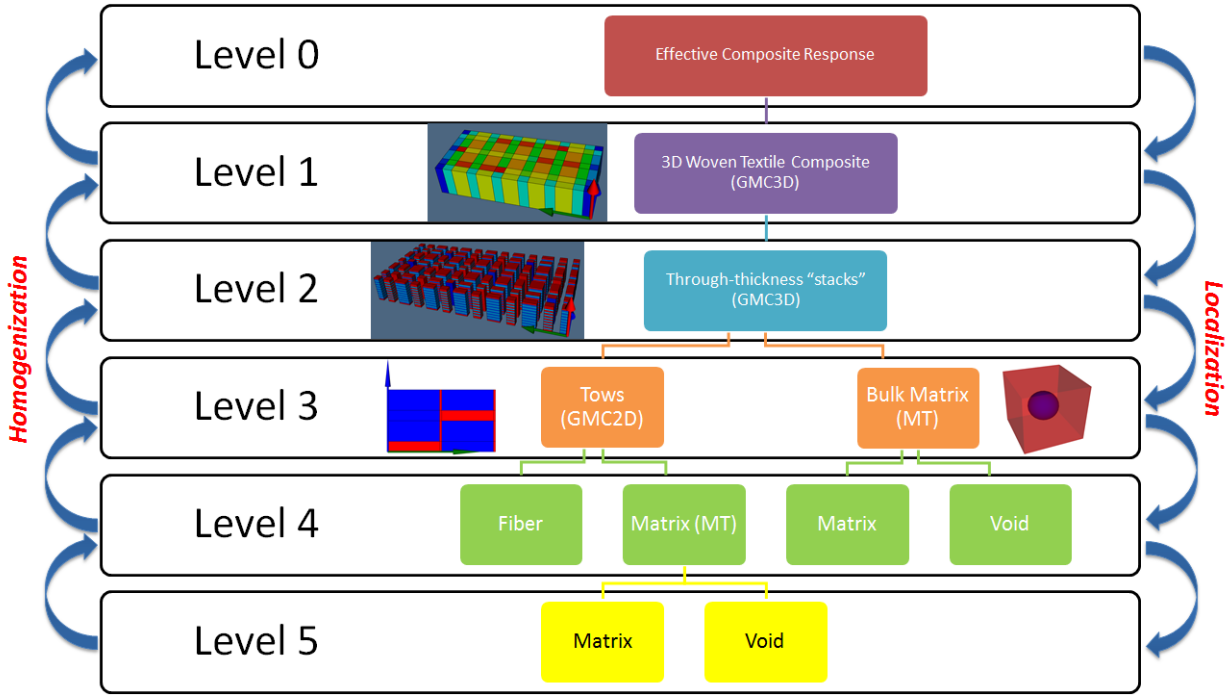

Figure 6. MsRM RUC hierarchy deployed to model the SN005 3D woven CFRP within NASMAT. Level 0 – Macroscale. Level 1 – Mesoscale. Level 2 – Stack-scale. Level 3 – Microscale. Level 4 – Constituent-scale. Level 5 – Subscale.

Referring to Figure 6, Level 0 which is the highest scale represent the macroscale of the composite. NASMAT computes the effective properties, as well as the fully 3D macroscopic stress and strain tensors considering the nonlinear effects from all the scales below.

The homogenization of the mesoscale is separated into two steps, called double-homogenization. At the next scale, Level 1, the mesoscale details of the 3D woven composite are represented with a single subcell through the thickness of the RUC and the effective properties from Level 2. Triply-periodic GMC is used to homogenize Level 1. At the stack-scale, Level 2, the details of the 3D weave are represented, and triply-periodic GMC is again used for the homogenization. Double-homogenization is employed to compensate for the lack of shear-normal coupling in GMC [39]. By homogenizing the stacks in Level 2 first, the effective properties in the subcells at Level 1 are anisotropic. Therefore, the normal-shear coupling is retained at Level 1 as an effect of the local constitutive response, as opposed to the arrangement of constituents.

Levels 1 and 2 are used to represent the idealized geometry presented in Figure 5. One advantage of using GMC is that the theory is insensitive to refinements in the discretization of the unit cell, for a fixed geometry. Therefore, the subcell grid with the least amount of subcells needed to represent the

desired geometry can be utilized. This is because the continuity conditions used to formulate the strain concentration matrix, which maps the global strains to the local strains, is enforced in an average, integral sense. This results in the directional volume fractions being the contributing factor in the homogenization, not local spatial location [40]. Thus, some the challenges normally associated with meshing these complex architectures are eliminated for an idealized geometry [41]. Imperfect, or "non-ideal," geometries a can be considered by altering the idealized RUC, as appropriate.

The effective constitutive properties of the subcells in the stacks are computed via the homogenization of the bulk matrix containing voids, using MT, and the homogenization of a 4 x 4 RUC of hexagonally packed fibers in tow, using doubly-periodic GMC, at Level 3 – the microscale. Stress concentration due to the presence of the square fiber in the 4x4 RUC are not captured for the same reasons that GMC is not sensitive to grid refinement. At Level 4 (the constituent scale), the material properties of the base fiber constituent at the current time are provided to Level 3 along with the effective properties of the inter-tow matrix, obtained using MT. In addition, the effective properties of the base matrix constituent, and the spherical void, are provided to the Level 3 MT model of the bulk matrix. Details of how the properties of the void are treated are given in the "Material Properties" subsection. Finally, the Level 5 subscale consists of just the base matrix and void constituents, the properties of which are used in the Level 4 MT model of the inter-tow matrix.

The baseline MsRM NASMAT model contains a total of 6,672 GMC subcells and 27,114 MT phases (voids or matrix). A total of 14,760 homogenizations are performed each time step, 13,557 of which use MT. The model is subjected to six uniaxial load cases with the specified uniaxial strain being applied over 100 time steps. The average computation time for each simulation using a single CPU on a Windows machine is on the order of ~30 seconds.

Subcell Failure Model

Material non-linearity is introduced into the model in the form of material failure. Maximum stress and maximum strain failure criteria were specified for the fiber constituent that considers only the normal components of stress or strain.

$$\max\left(\left\|\frac{\sigma_i^{(\alpha_f\beta_f\gamma_f)}}{X_f}\right\|,\left\|\frac{\varepsilon_i^{(\alpha_f\beta_f\gamma_f)}}{X_f^{\varepsilon}}\right\|\right)\geq 1, \qquad \sigma_i^{(\alpha_f\beta_f\gamma_f)}>0, \qquad i=1,2,3 \tag{12}$$

where $\sigma_i^{(\alpha_f\beta_f\gamma_f)}$, $\varepsilon_i^{(\alpha_f\beta_f\gamma_f)}$ are the normal components of stress and strain in the a fiber subcell, and X_f, X_f^{ε} are the stress and strain allowables for the fiber. For the matrix, a maximum stress criterion was also applied, but all stress components were considered.

$$\max\left(\left\|\frac{\sigma_i^{(\alpha_m\beta_m\gamma_m)}}{X_m}\right\|,\left\|\frac{\tau_{ij}^{(\alpha_m\beta_m\gamma_m)}}{Y_m}\right\|\right)\geq 1, \qquad \sigma_i^{(\alpha_m\beta_m\gamma_m)}>0, \qquad i=1,2,3, \quad i\neq j \tag{13}$$

where $\sigma_i^{(\alpha_m\beta_m\gamma_m)}$ and $\tau_{ij}^{(\alpha_m\beta_m\gamma_m)}$ are the normal and shear stresses in a matrix subcell, and X_m and Y_m are the normal and shear stress allowables for the matrix. Upon satisfaction of Eq. (12) or (13), a very simple "subvolume elimination" damage model has been used, wherein, the stiffness of the failed

subcell is set to a very low value (in all directions). Only constituent materials, which are at the lowest scales (Levels 5 and 6) in the MsRM hierarchy (see Figure 6) are allowed to fail. The local failure event is discrete. Yet, the effective damaging response at the macroscale is progressive as the subcell failure advances locally, and the nonlinear effects of failure percolate up the scales through the homogenized stiffness tensors.

Geometry Details and Material Properties

The SN005 panel was composed of AS4-6k carbon fiber tows and RTM6 epoxy matrix. The minimum number of elastic constants used to compute the stiffness tensor of these phases is given in Table I. The stiffness for the void was given an extremely low value. The failure criterion allowables for the fiber and matrix used in Eq. (12) and (13) are given in Table II.

TABLE I. ELASTIC PROPERTIES OF AS4 FIBER AND RTM6 MATRIX.

AS4 Fiber Property		RTM6 Matrix Property	
E_{11} (GPa)	231	E	2.89
E_{22} (GPa)	15.0	v	0.35
v_{23}	0.3		
v_{12}	0.21		
G_{12} (GPa)	15.8		

TABLE II. FAILURE CRITERION ALLOWABLES.

Allowable	
X_f (GPa)	3.35
X_f^{ε}	0.015
X_m (MPa)	75.0
Y_m (MPa)	49.1

The local fiber volume fraction used in the GMC RUC tows at Level 3 (see Figure 6) is 80% which results in a global fiber volume fraction of 50.3%. X-Ray CT images of the flat panels in Figure 2 do not indicate that voids are relevant manufacturing-induced defects. However, the results from acid digestions tests suggest that the void content is 0.4%, and therefore must be in the form of distributed voids or porosity. The local void content of the MT models is prescribed to be 0.805% which yields a global 0.4% distributed void content in the 3D woven RUC. Due to the idealization of the geometry, the global fiber volume fraction does not exactly match the fiber volume content measure from the acid digestion tests; however the global void content is accurate [12].

Modeling Localized Voids with MsRM

It is apparent from Figure 3 that, more complex geometries can result in localized voids arising in the as manufactured part. One focus of the current work is to use NASMAT to estimate the sensitivity of the stress-strain response to such defects. A location were the formation of voids is observed in Figure 3 is in the matrix regions between tows. To simulate the effects of these localized voids a matrix subcell, in the middle of two tows within a Level 2 (see Figure 6) stack, is chosen, and the volume fraction of the spherical void in the Level 3 MT model linked to this subcell is substantially increased. To isolate the effects of the localized void, the distributed voids ae removed from the model. The local volume fraction of the voids in the remaining MT model is increased to 46% such that the global void content remains at 0.4%.

Two cases are considered: A localized void between two warp tows or between two weft tows. The same stack definition is linked to multiple subcells at the Level 1 mesoscale to represent the idealized weave pattern. Thus, there are numerous localized voids distributed throughout the MsRM model. When the void is placed between two warp tows, the repetitive use of of the stack definition is such that there are 12 local voids. There are eight local voids when it is located between two weft tows. Since the voids are not distributed, the global volume fraction is not the measure controlling the response of the RUC. But rather, it is the driving by the local void content. Therefore local void content is kept constant for the two scenarios.

Modeling Through-thickness Binder tow Disbonds with MsRM

As mentioned previously, disbonding of the binder tows in the warp direction as they traverse the composite in the through-thickness (TT) direction, is a prominent observed defect in the 3D woven AS4/RTM6 composite. Typical binder tow disbonds present in the as-manufactured AS4/RTM6 composite are shown in Figure 2. To model the effect of such preexisting disbonds on the mechanical response of the composite, a different GMC representation of the through thickness section of the binder tows has been defined. That is, the binder tows running in the warp direction, at the top and bottom of the composite, have not been redefined. The new TT binder tow definition includes a thin subcell (adjacent in the x_3-direction) that traverses the entire thickness with very low mechanical properties. This disables the ability of the TT binder tow to transfer any traction in the x_3-direction (warp), see Figure 6. This has been applied to all six TT binder tows and thus represents an upper bound for the effect of the TT binder tow disbonds on the composite response. In the context of the MsRM model of the composite, the thin void is added adjacent to the homogenized through-thickness stack of subcells representing the TT binder tow, essentially forming a new level between the mesoscale (Level 1) and the stack-scale (Level 2) where at the locations where there are binder tows, shown in Figure 5 and Figure 6.

RESULTS AND DISCUSSION

Baseline Prediction and Validation

The baseline model contains a global void content of 0.4% distributed throughout the matrix in the MsRM hierarchy shown in Figure 6. The predicted warp-direction (x_3, see Figure 5) stress/strain curve is compared to experimental data in Figure 7. Good agreement between the simulated and experimentally observed stress/strain curves were obtained with minimal analysis assumptions. The predicted warp-direction tensile modulus (59.3 GPa) and tensile strength (753 MPa) are both within 3% of experimental data. There is a sharp drop in the stress-strain curve at 343 MPa due to failure in bulk matrix. It is possible that an improved representation of the damage evolution in the subcells, via an energy-based continuum damage model, could slow the progression of failure in the bulk matrix and improve the ultimate strain to failure prediction.

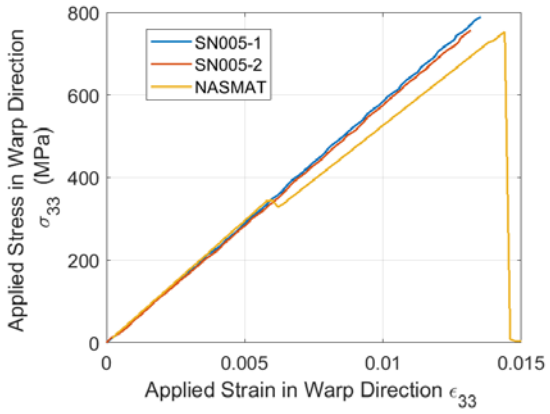

Figure 7. Warp-direction stress vs. strain prediction compared to experimental data.

Six uniaxial, applied strain simulations were conducted to obtain six directional strength predictions for the 3D woven CFRP. These strengths are summarized in Table III, and have yet to be validated (with the exception of the prediction of the ultimate stress in the warp-direction). Two values are presented in Table III. The damage initiation stress is the stress at which the stress-strain response predicted by the simulation deviates from linear, and the ultimate stress is the stress achieved in the entire global stress-strain history. The results in Table III indicate the weft-direction exhibits a lower damage initiation stress than the warp-direction, but a higher ultimate stress. The TT and in-plane shear strengths are predicted to be significantly lower than the in-plane normal strengths, in which the fiber axis is the direction of the primary load path.

TABLE III. PREDICTED STRENGTHS FOR 3D WOVEN COMPOSITE RUC WITH 0.4% DISTRIBUTED VOIDS.

Loading	Damage Initiation Stress (MPa)	Ultimate Stress (MPa)
ε_{11} (through-thickness)	14.7	55.3
ε_{22} (weft)	224	814
ε_{33} (warp)	343	753
γ_{23} (in-plane shear)	7.1	23.5
γ_{13} (transverse shear)	38.2	38.2
γ_{12} (transverse shear)	40.8	40.8

In Figure 8, the stress strain curves predicted for all six loading scenarios are presented. On the same axes, the volume of a failed constituent relative to the total volume of that constituent in the bulk matrix, warp tow, weft tow, and binder tow is plotted as a function of the applied strain. The value of the relative failed volume does not indicate the severity of the damage because the relationship between failed volume and stiffness degradation is not one-to-one. However, these plots provide a good qualitative sense of how the failure modes are evolving in the simulation.

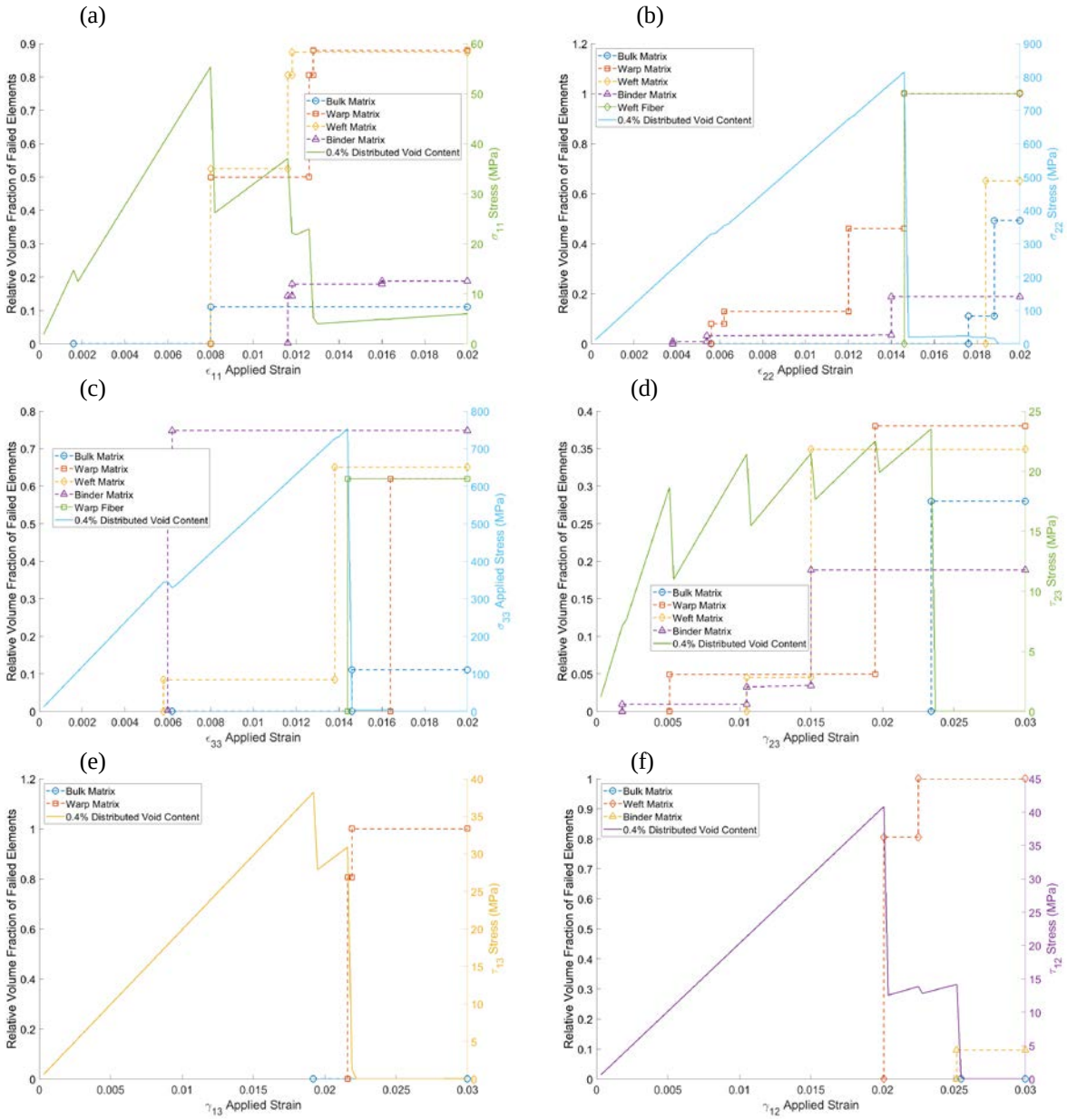

Figure 8. Evolution of relative volume fraction of failed constituents and stress-strain response for 3D woven composite RUC containing 0.4% distributed voids. a.) Applied ε_{11} (through-thickness) strain. b.) Applied ε_{22} (weft) strain. c.) Applied ε_{33} (warp) strain. d.) Applied γ_{23} (in-plane shear) strain. e.) Applied γ_{13} (transverse shear). f.) Applied γ_{12} (transverse shear).

Figure 8a shows results for an applied strain in the through-thickness direction. The simulation predicts that damage initiates due to cracking in the bulk matrix. Later warp matrix and weft matrix damage leads to a catastrophic drop in the load carrying capability of the composite. The damage evolution is dominated by matrix cracking. The fact that the binders do not contribute to the through-thickness strength, is an artifact of GMC. Once the bulk matrix subcell in the stacks containing the binders fail, those stacks can no longer sustain any load due to the lack of normal-shear coupling in GMC.

The simulated non-linear behavior of the 3D woven unit cell, when loaded in the weft x_2-direction, is displayed in Figure 8b. Matrix failure starts in the binder, but does note manifest as a noticeable drop in the stress-strain curve until the warp matrix fails. These two failure modes represent transverse cracking in the warp and binder tows. Ultimate failure is governed by fiber failure in the weft tows, as expected.

In the warp-direction, Figure 8c show that NASMAT predicts that matrix failure in the weft tow, binder tow, and intra tow region leads to an initial drop in the stress strain curve. Just prior to the ultimate failure there is some more weft matrix cracking, and the specimen fails catastrophically when the warp tow fibers fail. A similar failure mode evolution has been observed in multiscale finite element method simulations of similar 3D woven configurations [14].

Figure 8d shows the failure prediction under in-plane shear loading. Matrix damage accrues in the binder, followed by the warp tow, and the weft tow. The sudden loss of shear stiffness in the matrix results in the "saw-tooth" like pattern in the shear stress-shear strain curve. The local use of a progressive damage model would results in a much smoother non-linear curve.

The through-thickness shear response is exhibited in Figure 8e and Figure 8f. The response of these curves is dominated by the first subcell failure for the same reasons as when the RUC is loaded in the x_1-directon. Once there is a failure in a stack, the through-thickness reinforcement in that no longer holds any stress. Using the high fidelity GMC (HFGMC) to model the RUCs at the stack-scale, see Figure 6, may be a viable solution to this problem because the normal shear coupling that is lost due to the first order displacement approximation used in GMC will be recovered [37].

Effect of Distributed Void Content

TABLE IV. PERCENT DIFFERENCE IN STRENGTH BETWEEN 3D WOVEN COMPOSITE RUC WITH NO VOIDS AND BASELINE MODEL CONTAINING 0.4% DISTRIBUTED VOIDS.

Loading	%Diff. Damage Initiation Stress	%Diff. Ultimate Stress
ε_{11} (through-thickness)	1.3	-1.1
ε_{22} (weft)	0.083	0.056
ε_{33} (warp)	0.083	0.027
γ_{23} (in-plane shear)	0.87	1.4
γ_{13} (transverse shear)	1.3	1.3
γ_{12} (transverse shear)	1.3	1.3

TABLE V. PREDICTED DIFFERENCE IN STRENGTH BETWEEN 3D WOVEN COMPOSITE RUC WITH 10X INCREASE IN VOID CONTENT AND BASELINE MODEL CONTAINING 0.4% DISTRIBUTED VOIDS.

Loading	%Diff. Initiation Stress	%Diff. Ultimate Stress
ε_{11} (through-thickness)	-11	-10
ε_{22} (weft)	-11	-0.41
ε_{33} (warp)	-7.6	1.8
γ_{23} (in-plane shear)	-7.7	-6.6
γ_{13} (transverse shear)	-8.5	-8.5
γ_{12} (transverse shear)	-7.2	-7.2

The baseline model for the S500 coupon contained 0.4% void content distributed throughout the bulk and intertow matrix. It is of interest to see if this amount of as-manufactured voids, or porosity, has any effect on the strengths of the material. Simulations were conducted with MsRM RUCs that contained no voids by replacing the MT models at Levels 3 and 4 with pure matrix. Table IV shows that there is less than 2% percent difference in the predicted strengths for the RUC with no voids

compared to the baseline with 0.4% distributed void content. Similarly, the removal of voids did not change the evolution of the damage mechanisms in any of the cases.

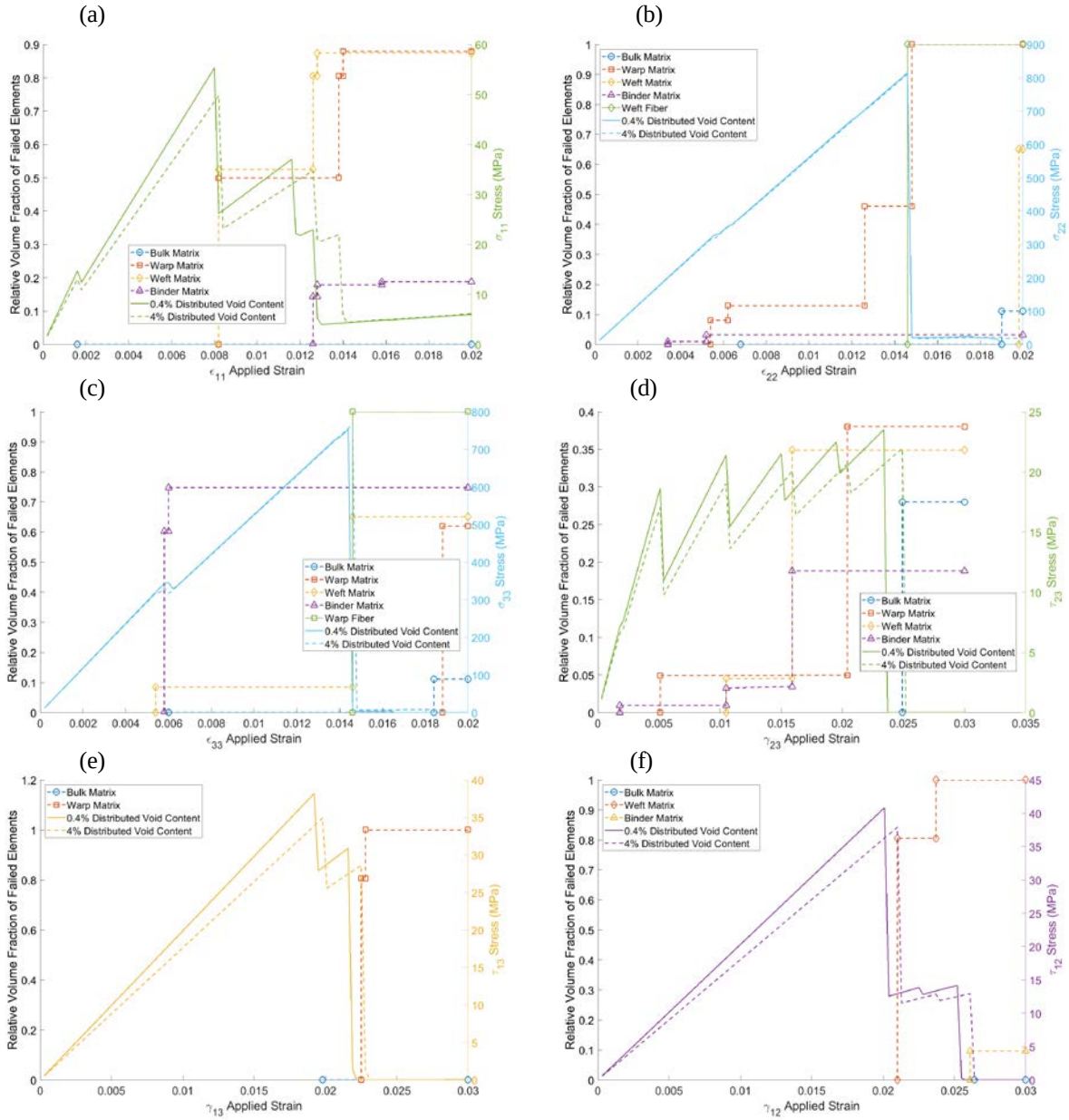

Figure 9. Evolution of relative volume fraction of failed constituents and comparison of stress-strain response of 3D woven composite RUC with 10x increase in void content to baseline simulation containing 0.4% distributed voids. a.) Applied ε_{11} (through-thickness) strain. b.) Applied ε_{22} (weft) strain. c.) Applied ε_{33} (warp) strain. d.) Applied γ_{23} (in-plane shear) strain. e.) Applied γ_{13} (transverse shear). f.) Applied γ_{12} (transverse shear).

To discern if the composite strengths are sensitive to the presence of distributed voids, the global void content was amplified by an order of magnitude to 4% which required a local void content of 8.05%. A distributed void, or porosity content of 4% is plausible if the part geometry is complex and/or a different resin system is used.

Table V summarized the difference in the predicted strengths between the baseline RUC and an RUC with 10 times the distributed void content. This result in as high as ~10-11% change in the initiation and ultimate stresses. The minimum difference in observed damage initiation stress was ~7%. Yet, the increased porosity had no effect on the ultimate strength in the weft direction. Most models exhibited a change of ~6-8% in the initiation and final strength. All cases showed the increased porosity led to a decrease in the observed strengths, except for the ultimate strength in the warp direction.

The complete stress-strain curves for all six uniaxial loading configurations are presented in Figure 9. It is clear that, for the cases with a substantial knockdown in ultimate strength, the difference is a result of change in the global stiffness due to the increased porosity. The strain to failure displays far less deviation from the baseline case. None of the plots in Figure 9 show a difference in the evolution of the failure modes.

Effect of Localized Voids

Motivated by the X-Ray CT scans in Figure 2 and acid digestion tests, voids were modeled in the previous section as distributed porosity. However Figure 3 shows that for more complex geometries, the manufacturing process results in large localized voids. The predicted strengths of 3D woven RUCs containing localized voids is presented in this section.

The six strengths of the RUC with localized voids between the weft tow predicted under uniaxial strains are summarized in Table VI. The through-thickness strengths were the most influenced by the presence of the local voids, especially the transverse shear strengths. The 12-shear strength exhibited a 44% reduction. There is most likely significant error in the value of this reduction. Still, a marked reduction in the through-thickness shear strengths of a 3D woven composite is plausible, and expected, because the missing matrix adjacent to a weft tow would allow for easier rotation of that tow, inducing other local stresses throughout the material. Localizing the void content did not significantly affect the progression of failure modes. Similar trends in the strengths (Table VII) are observed when the local voids are placed in between warp tows. However, the 13-shear strength is more significantly impacted than the 12-strength, opposite of the previous set of results.

TABLE VI. PREDICTED PERCENT DIFFERENCE IN STRENGTH OF 3D WOVEN COMPOSITE RUC LOCALIZED VOIDS BETWEEN WEFT TOWS COMPARED TO BASELINE MODEL CONTAINING DISTRIBUTED 0.4% VOIDS.

Loading	%Diff. Damage Initiation Stress	%Diff. Ultimate Stress
ε_{11} (through-thickness)	0.37	-4.8
ε_{22} (weft)	0.07	-0.047
ε_{33} (warp)	0.07	0.023
γ_{23} (in-plane shear)	0.08	-6.0
γ_{13} (transverse shear)	-12	-12
γ_{12} (transverse shear)	-44	-44

TABLE VII. PREDICTED PERCENT ERROR IN STRENGTH OF 3D WOVEN COMPOSITE RUC LOCALIZED VOIDS BETWEEN WARP TOWS COMPARED TO BASELINE MODEL CONTAINING DISTRIBUTED 0.4% VOIDS.

Loading	%Error Damage Initiation Stress	%Error Ultimate Stress
ε_{11} (through-thickness)	-0.08	-2.9
ε_{22} (weft)	5.3	0.13
ε_{33} (warp)	-0.92	-1.0
γ_{23} (in-plane shear)	0.71	1.1
γ_{13} (transverse shear)	-34	-34
γ_{12} (transverse shear)	-9.4	-9.4

Effect of Disbonds in the Through-Thickness (TT) Binder Tow

The differences between the simulations with and without the TT binder tow disbond, in terms of the predicted damage initiation stress and ultimate stress, are shown in Table VIII. Because the binder tow disbond is normal to the x_3-direction (see Figure 2 and Figure 3), its effect on the through-thickness (x_1-) direction and the weft (x_2-direction) direction normal stress-strain responses is minimal (see Figure 10a and Figure 10b). As one would expect, the effect in the warp (x_3-) direction (see Figure 10c) is more significant. The initial warp-direction Young's modulus is decreased by 8%, and the effect of the damage initiation event (partial failure of the weft matrix) is muted compared to the baseline case. However, after this damage initiation event, the curve that includes the binder tow disbonding follows the baseline stress-strain curve closely, and the predicted ultimate stress, which is associated with warp fiber failure, is nearly identical. Clearly, because the TT binder tows carry very little stress when the composite is loaded in the warp direction and the final is dictated by warp fiber failure, the TT binder tow disbond has minimal effect.

TABLE VIII. PREDICTED PERCENT DIFFERENCE IN STRENGTH OF 3D WOVEN COMPOSITE RUC WITH TT BINDER TOW DISBONDING COMPARED TO BASELINE MODEL CONTAINING DISTRIBUTED 0.4% VOIDS.

Loading	%Diff. Initiation Stress	%Diff. Ultimate Stress
ε_{11} (through-thickness)	-1.8	-3.4
ε_{22} (weft)	-0.12	-0.051
ε_{33} (warp)	-11	0.15
γ_{23} (in-plane shear)	N.A.	N.A.
γ_{13} (transverse shear)	-19	-19
γ_{12} (transverse shear)	-0.0072	-0.0072

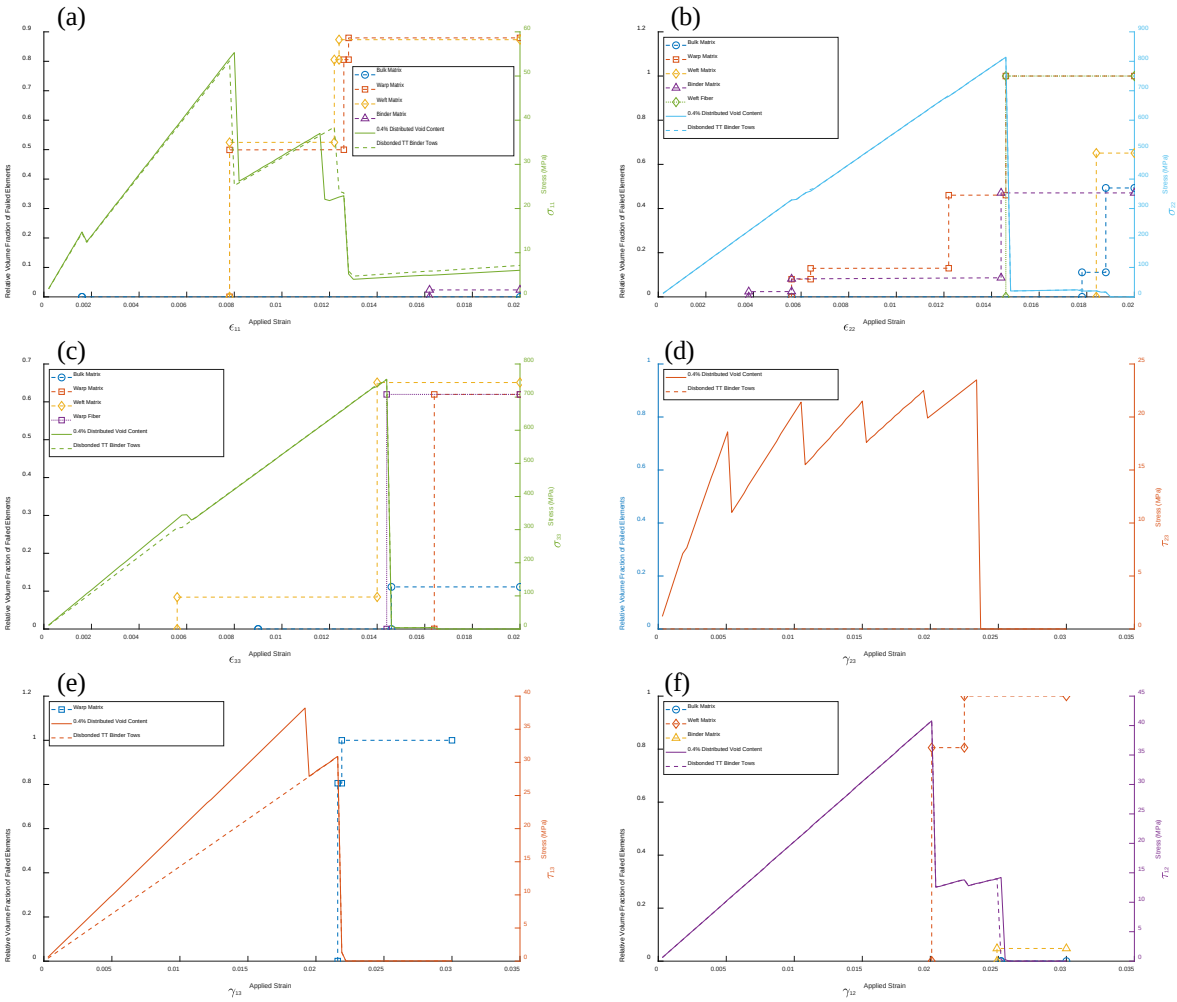

Figure 10. Evolution of relative volume fraction of failed constituents and comparison of stress-strain response of 3D woven composite RUC with TT binder tow disbonds compared to baseline simulation containing 0.4% distributed voids. a.) Applied ε_{11} (through-thickness) strain. b.) Applied ε_{22} (weft) strain. c.) Applied ε_{33} (warp) strain. d.) Applied γ_{23} (in-plane shear) strain. e.) Applied γ_{13} (transverse shear). f.) Applied γ_{12} (transverse shear).

Figure 10d, indicates that adding the binder tow disbond through the entire thickness of the 3D woven composite completely eliminates the in-plane (x_2-x_3) shear stiffness. As previously discussed, this is because of the well-known lack of shear coupling within the GMC theory being used at Level 1 (see Figure 6) in the employed MsRM approach. This is obviously unrealistic and can be overcome by reducing the extent of the disbond or employing the HFGMC micromechanics theory [37].

The TT shear response curves are shown in Figure 10e and Figure 10f. While the τ_{12}-γ_{12} response (Figure 10f) is insensitive to the presence of the binder tow disbond, the τ_{13}-γ_{13} response (Figure 10e) is significantly impacted. The initial shear modulus is reduced by 28%, and the ultimate stress is reduced by 19%. This is again due to the orientation of the disbond, normal to the x_3-direction and the lack of normal shear coupling may be a contributor to the severity.

CONCLUSION

The MsRM method utilizing GMC and MT was deployed using the NASMAT computational framework to predict the stress-strain response of a 3D woven CFRP woven unit cell containing as manufactured distributed voids and subjected to uniaxial loads. The ultimate strength in the warp direction was predicted to within 3% of experimental data, and the evolution of the failure modes were aligned with those reported in the literature obtained using higher fidelity, multiscale FEM models. The simulation results provide insight into the damage tolerant nature of 3D woven composites. Although initial matrix damage occurs and can be observed in the global stress-strain response of the composite, the cracks are not allowed to progress and develop into critical flaws. Catastrophic failure does not occur until much later, as a result of fiber fracture. In addition, the in-plane damage tolerance of the 3D woven material was demonstrated because of its ability to carry substantial load in the presence of porosity, voids, and TT binder tow disbonds.

Reasonable predictions for the weft and in-plane shear behavior of the 3D woven unit cell are presented. However, these results still need to be validated experimentally. The through-thickness strength predictions contain error due to the well-known lack of normal-shear coupling with GMC. This can be remedied by employing HFGMC selectively throughout the MsRM model without severely affecting the computational cost.

Parametric studies were conducted to ascertain the influence of increased porosity and localized voids. There was no discernable difference between in the strengths when distributed voids were removed. The void content was increased to 10 times the measured data which lead to a noticeable decrease in the damage initiation stress, but not the ultimate strength, in the warp and weft directions. However, it did affect both initiation and ultimate strengths under in-plane shear loading. The effect of localized voids on the in-plane strengths were minimal. Except when voids between the weft tows led to a 6% reduction in the in-plane ultimate shear strength, and voids between warp tows led to a 5.3% increase in the weft direction damage initiation stress.

The effect of disbonding of the TT binder tows was also simulated. The in-plane (τ_{23}-γ_{23}) shear response did show sensitivity to the TT binder disbond but this simulations was not realistic because the simulated disbond spanned the entire composite thickness. Also, the fact that the employed GMC micromechanics theory lacks shear coupling increased the apparent severity of the disbond. Omitting the through thickness strengths for aforementioned reasons, none of these defects had a significant effect on the warp or weft ultimate strengths of the material. The warp tensile results were noteworthy as, in this case, even though the disbond was oriented normal to the loading direction and affected the initial slope and damage initiation stress, the ultimate stress prediction was not significantly affected. This is because, even without the disbond, very little stress is carried by the TT binder tows in response to in-plane normal loading.

The predictive capability of NASMAT combined with its speed provides an attractive tool for performing rapid engineering trade studies on complex composite systems. This example also demonstrates NASMAT's flexibility by incorporating five separate levels of calculations and three distinct micromechanics theories under one platform. This development addresses an apparent technological gap observed in the open literature. There exists very few modeling tools that can delve below the meso-scale of 3D woven composites; although, this may be a requirement necessary to capture the physics of damage at the appropriate length scale. Deficiencies to predict the through-thickness behavior of the 3D woven composite were identified in the specific MsRM strategy used for this work, and a solution involving the inception of HFGMC into the workflow has been proposed.

ACKNOWLEDGEMENTS

The authors would like to thank the NASA Composites Technology for Exploration (CTE) project under the Game Changing Development program in the Space Technology Mission Directorate for supporting this work. They would also like to thank Dr. Cheryl Rose and Dr. Andrew Bergan for their help with the X-Ray CT work.

REFERENCES

1. Cox, B. N., M. S. Dadkhah, W. L. Morris, and J. G., Flintoff. 1994. "Failure Mechanisms of 3D Woven Composites in Tension, Compression, and Bending," *Acta Metall. Mater.*, 42(12), pp. 3967-3984.
2. Brandt, J., K. Drechsker, and F.-J. Arendts. 1996. "Mechanical Performance of Composites Based on Various Three-Dimensional Woven-Fibre Preforms," *Compos. Sci. Technol.*, 56, pp. 381-386.
3. Kuo, W.-S., J. Fang, and H.-W. Lin. 2003. "Failure Behavior of 3D Woven Composites Under Transverse Shear," *Compos. Part A Appl. Sci. Manuf.*, 34, pp. 561-575.
4. Gerlach, R., C. R. Siviour, J. Wiegand, and N. Pertinic. 2012. "In-plane and Through-thickness Properties, Failure Modes, Damage and Delamination in 3D Woven Carbon Fibre Composites Subjected to Impact Loading," *Compos. Sci. Technol.*, 72, pp. 397-411
5. Potluri, P., P. Hogg, M. Arshad, D. Jetavat, and P. Jamshidi. 2012. "Influence of Fiber Architecture on Impact Damage Tolerance in 3D Woven Composites," *Appl. Compos. Mater.*, 19, pp. 799-812.
6. Dai, S., P. R. Cunningham, S Marshall, and C. Silva. 2015. "Influence of Fibre Architecture on the Tensile, Compressive and Flexural Behaviour of 3D Woven Composites," *Compos. Part A Appl. Sci. Manuf.*, 69, pp. 195-207.
7. Warren, K. C., R. A. Lopez-Anido, and J. Goering. 2015. "Experimental Investigation of Three-dimensional Woven Composites," *Compos. Part A Appl. Sci. Manuf.*, 73, pp 242-259.
8. Yan, S., X. Zeng, and A. Long. 2018. "Experimental Assessment of the Mechanical Behaviour of 3D Woven T-joints," *Compos. Part B-Eng.*, 154, pp. 108-113.
9. Mahadik, Y., S. R. and Hallet. 2011. "Effect of Fabric Compaction and Yarn Waviness on 3D Woven Composite Compressive Properties," *Compos. Part A Appl. Sci. Manuf.*, 42, pp. 1592-1600.
10. Tsukrov, I., H. Bayraktar, M. Giovinazzo, J. Goering, T. Gross, M. Fruscello, and L. Martinsson. (2011). "Finite Element Modeling to Predict Cure-induced Microcracking in Three-dimensional Woven Composites," *Int. J. Fract.*, 172, pp. 209-216.
11. Potter, E., S. T. Pinho, P. Robinson, L. Iannucci, and A. J. McMillan. 2012. "Mesh Generation and Geometrical Modelling of 3D Woven Composites with Variable Tow Cross-Sections," *Comput. Mater. Sci.*, 51, pp. 103-111.
12. Farrokh, B., K. N. Segal, T. M. Ricks, S. G. Miller, B. T. Rodini, and D. S. Sleight. 2019. "Uniaxial Tensile Properties of AS4 3D Woven Composites with Four Different Resin Systems: Experimental Results and Analysis – Property Computations," presented at the Composites and Advanced Materials Expo (CAMX), September 23-26, 2019, Anaheim, CA.
13. Jones, J. S., D. L. Polis, R. R. Rowles, and K. N. Segal, 2011. "Comparative study of 3-Dimensional Woven Joint Architectures for Composite Spacecraft Studies," presented at the Society for the Advancement of Material Process Engineering (SAMPE) Conference, May 22-26, 2011, Long Beach, CA.
14. Dai, S., and P. R. Cunningham. 2016. "Multi-scale Damage Modelling of 3D Woven Composites Under Uni-axial Tension," *Compos. Struct.*, 142, pp. 298-312.
15. Liu, G., L. Zhang, Guo, L., Lioa, F., Zheng, T., and S. Zhong. 2019. "Multi-scale Progressive Failure Simulation of 3D Woven Composites under Uniaxial Tension," *Compos. Struct.*, 208, pp. 233-243.
16. Green, S. D., M. Y. Matveev, A. C. Long, D. Ivanov, and S. R. Hallett. 2014. "Mechanical Modelling of 3D Wvoen Composites Considering Realistic Unit Cell Geometry," *Compos. Struct.*, 118, pp. 284-293.
17. Zhang, D., A. M. Waas, and C. –F. Yen. 2015. "Progressive Damage and Failure Response of Hybrid 3D Textile Composites Subjected to Flexural Loading, Part II: Mechanics Based Multiscale Computational Modeling of Progressive Damage and Failure," *Int. J. Solids. Struct.*, 75-76, pp. 321-225.
18. Patel, D. K., A. M. Waas, and C. -F. Yen. 2018. "Direct Numerical Simulation of 3D Woven Textile Composites Subjected to Tensile Loading: An Experimentally Validated Multiscale Approach," *Compos. Part B-Eng.*, 152, pp. 102-115.

19. Joglekar, S., and M. Pankow. 2017. “Modeling of 3D Woven Composites using the Digital Element Approach for Accurate Prediciton of Kinking under Compressive Loads,” *Compos. Struct.*, 160, pp. 547-559.
20. Lu, H., L. Guo, G. Liu, and L. Zhang. 2018. “A Progressive Damage Model for 3D Woven Composites under Compression,” *Int. J. Damage Mech.*, 28 (6), pp. 857-876.
21. Warren, K. C., R. A. Lopez-Anido, S. S. Vel, and H. H. Bayraktar. 2016. “Progressive Failure Analysis of Three-dimensional Woven Carbon Composites in Single-bolt, Double-shear bearing,” *Compos. Part B-Eng.*, 84, pp. 266-276.
22. Yan, S., X. Zeng, and A. Long. 2019. “Meso-scale Modeling of 3D Woven Composite T-joints with Weave Variations,” *Compos. Sci. Technol.*, 171, pp. 171-179.
23. Yen, C.-F., and B. Boesl. 2011. “Progressive Failure Micromechanical Modeling of 3D Woven Composites,” presented at 52nd AIAA/ASME/ASCE/AHS/ASC Structures, Structural Dynamics and Materials Conference, April 4-7, 2011, Denver, CO.
24. Pankow, M., A. M. Waas, C.F. Yen, and S. Ghiorse. 2012. “Modeling the Response, Strength and Degradation of 3D Woven Composites Subjected to High Rate Loading,” *Compos. Struct.*, 94(5), pp. 1590-1604.
25. Elias, A., F. Laurin, M. Kaminski, and L. Gornet. 2017. “Experimental and Numerical Investigations of Low Energy/Velocity Impact Damage Generated in 3D Woven Composite with Polymer Matrix,” *Compos. Struct.*, 159, pp. 228-239.
26. Huang, T., and Y. Gong. 2018. “A Multiscale Analysis for Predicting the Elastic Properties of 3D Woven Composites Containing Void Defects,” *Compos. Struct.*, 185, pp. 401-410.
27. Wang, Q., T. Li, X. Yang, Q. Huang, B. Wang, and M. Ren. 2020. “Multiscale Numerical and Experimental Investigation Into the Evolution of Process-induced Residual Strain/Stress in 3D Woven Composites,” *Compos. Part A Appl. Sci. Manuf.*, 135, 105913.
28. Stig, F., and S. Hallström. 2013. “Influence of Crimp on 3D-woven Fibre Reinforced Composites,” *Compos. Struct.*, 95, pp. 114-122.
29. Chen, X., 2011. “Mathematical Modelling of 3D Woven Fabric for CAD/CAM Software,” *Text. Res. J.*, 81(1), pp. 42-50.
30. Drach, A., B. Drach, and I. Tsukrov. 2014. “Processing of Fiber Architecture Data for Finite Element Modeling of 3D Woven Composites,” *Adv. Eng. Softw.*, 72, pp. 18-27.
31. Isart, N., B. El Said, D. A. Ivanov, S. R. Hallett, J. A. Mayugo, and N. Blanco. 2015. “Internal Geometric Modelling of 3D Woven Composites: A Comparison between Different Approaches,” *Compos. Struct.*, 132, pp. 1219-1230.
32. Wintiba, B., B. Sonon, K. Ehab Moustafa Kamel, and T. J. Massart. 2017. “An Automated Procedure for the Generation and Conformal Discretization of 3D Woven Composites,” *Compos. Struct.*, 180, pp. 955-971.
33. Mendoza, A., J. Schneider, E. Parra, and S. Roux. 2019. “The Correlation Framework: Bridging the Gap between Modeling and Analysis for 3D Woven Composites,” *Compos. Struct.*, 229, 111468.
34. Ewart, A., B. Drach, K. Vasylevski, and I. Tsukrov. 2020. “Predicting the Overall Response of an Orthogonal 3D Woven Composite using Simulated Tomography-Derived Geometry,” *Compost. Struct.*, 243, 112169.
35. Bergan, A. C. 2020. “An Automated Meshing Framework for Progressive Damage Analysis of Fabrics using CompDam,” presented at the American Society for Composites 35th Technical (Virtual) Conference, September 14-17, 2020.
36. Pineda, E. J., T. M. Ricks, B. A. Bednarcyk, and S. M. Arnold. 2020. “Software Architecture and Hierarchy of the NASA Multiscale Analysis Tool,” presented at The Conference on Advancing Analysis & Simulation in Engineering (CAASE20), June 16-18, 2020, Virtual Conference.
37. Aboudi, J., S. M. Arnold, and B. A. Bednarcyk. 2012. *Micromechanics of Composite Materials: A Generalized Multiscale Analysis Approach*. Butterworth-Heinemann.
38. Mura, T. 1982. *Micromechanics of Defects in Solids*. Martinus Nijhoff, The Hague.
39. Bednarcyk, B. A., and S. M. Arnold. 2003. “Micromechanics-based modeling of woven polymer matrix composites,” *AIAA J.*, 41(9), pp. 1788-1796.
40. Liu, K. C., and Ghoshal, A. 2014. “Inherent symmetry and microstructure ambiguity in micromechanics,” *Compos. Struct.*, 108, pp. 311-318.
41. Doitrand, A., C., C. Fagiano, F.-X. Irisarri, and M. Hirsekorn. “Comparison between Voxel and Consistent Meso-scale Models of Woven Composites,” *Compos. Part A Appl. Sci. Manuf.*, 73, pp. 143-154.